

Highly corrupted image inpainting through hypoelliptic diffusion *

Dario Prandi [†], Alexey Remizov [‡], Roman Chertovskih [§],
Ugo Boscain [¶], Jean-Paul Gauthier ^{||}

Abstract: We present a new image inpainting algorithm, the Averaging and Hypoelliptic Evolution (AHE) algorithm, inspired by the one presented in [1] and based upon a (semi-discrete) variation of the Citti–Petitot–Sarti model of the primary visual cortex V1. In particular, we focus on reconstructing highly corrupted images (i.e. where more than the 80% of the image is missing).

1 Introduction

In art, image inpainting refers to the practice of (manually) retouching damaged paintings in order to remove cracks or to fill-in missing patches. Within the past decade the digital version of image inpainting, i.e., the reconstruction of digital images by means of different types of automatic algorithms, has received increasing attention. It is out of the scope of this paper to provide a complete list of references on this problem. The references [2, 3, 4, 5, 6] concerns variational approaches that can be compared with our method.

The starting point of our work is the Citti–Petitot–Sarti model of the primary visual cortex V1 [7, 8, 9, 10], and our recent contributions [1, 11, 12, 13]. This model

has also been deeply studied in [14, 15, 16, 17]. The main idea behind the Citti–Petitot–Sarti model is the geometric model of vision called *pinwheel model*, going back to the 1959 paper [18]. Here, Hübner and Wiesel showed that cells in the mammals primary visual cortex V1 do not only deal with positions in the visual field, but also with orientation information: actually there are groups of neurons that are sensitive to position and directions with connections between them that are activated by the image. The system of connections between neurons, which is called the functional architecture of V1, preferentially connects neurons detecting alignments. This is the so-called pinwheels structure of V1. In the Citti–Petitot–Sarti model, V1 is then modeled as a 3D manifold endowed with a sub-Riemannian structure that mimics these connections as a continuous limit. The natural way to inpaint the missing regions of an image is thus by using the hypoelliptic diffusion naturally associated with this structure.

In [1] we proposed a semi-discrete version of the Citti–Petitot–Sarti model that considers a continuous structure in the space of position but a discrete structure for the orientation information, which could make sense from the neuro-physiological point of view. Image reconstruction methods based upon this principle are presented in detail in the previous works [12, 1]. Moreover, in [19], the same techniques are applied to the semi-discrete hypoelliptic evolution associated with the well-known Mumford elastica model.

In the above mentioned works, the main focus was on inpainting algorithms where no prior knowledge on the location of the corruption was needed. In this paper, on the contrary, we assume complete knowledge of the location and shape of the corrupted areas of the image. Exploiting this knowledge allows us to introduce certain heuristic procedures that together with the hypoelliptic diffusion drastically improve on the inpainting results.

Since no feedback from higher levels of the brain is assumed, and hence no copy-and-paste texture synthesis are allowed, the resulting algorithms cannot compete with state-of-the-art algorithms when treating large corruptions [2]. However, we show that our technique yields remarkable results when the corruptions are small but

*U. Boscain, J.-P. Gauthier, D. Prandi, and A. Remizov have been supported by the European Research Council, ERC StG 2009 “GeCoMethods” (contract 239748) and by the iCODE institute, research project of the Idex Paris-Saclay and by the EU FP7 project QUANT, grant agreement no. 297861. R. Chertovskih acknowledges financial support of the FAPESP, grant 2013/01242-8. D. Prandi was supported by the Laboratoire d’Excellence Archimède, Aix-Marseille Université

[†]LSIS, UMR CNRS 7296, Université de Toulon USTV, 83957, La Garde Cedex, France dario.prandi@gmail.com

[‡]CMAP, École Polytechnique CNRS, Route de Saclay, 91128 Palaiseau Cedex, France alexey-remizov@yandex.ru

[§]Department of Mathematics, Technological Institute of Aeronautics, Praça Marechal Eduardo Gomes 50, Vila das Acácias, 12228-900 São José dos Campos, SP – BRAZIL, kimor@ita.br

[¶]CNRS, CMAP, École Polytechnique CNRS, Route de Saclay, 91128 Palaiseau Cedex, France; INRIA Team GECO boscain@cmmap.polytechnique.fr <http://www.cmapx.polytechnique.fr/~char126/relaxboscain/>

^{||}LSIS, UMR CNRS 7296, Université de Toulon USTV, 83957, La Garde Cedex, France; INRIA Team GECO gauthier@univ-tln.fr <http://www.lsis.org/jpg>

quite dense in the total area of the image. Namely, we improve on the semi-discrete approach proposed in [1] for the Citti–Petitot–Sarti model, by introducing heuristic methods that allow us to treat images with more than 80% of corrupted pixels. These results are comparable with the state of the art and in particular with those obtained in [20] for an image with 65% of corrupted pixels, but no assumption of simple connectedness on the corrupted part is needed. Other unpublished results of S. Masnou with 83% of corruption are also comparable.

Exploiting a combination of our techniques and of copy-and-paste texture synthesis is outside the scope of this paper but is currently under investigation.

The paper is organized as follows.

- In the Section 2 we briefly recall the basic principles of the method introduced in [1, 12] and discuss some of its properties and present some results. In particular we present some numerical experiments showing the anisotropy of the diffusion. See Figures 2.1–2.3.
- In Section 3 we present a first improvement of this method, where an hypoelliptic diffusion with varying coefficients is considered. The coefficients are chosen for the effect of the anisotropic diffusion to be faster where the corruption is present. Final results on highly corrupted images obtained with this method appear on Figure 3.3.
- Section 4 contains the main result of this paper: the Averaging and Hypoelliptic Evolution (AHE) algorithm. Here, we combine the ideas coming from the Citti–Petitot–Sarti model and our contributions [12, 1], with some heuristic considerations in order to build an efficient image inpainting algorithm for highly corrupted images. This method is a synthesis of two different approaches to image reconstruction: the averaging method and the evolutionary method, based on the hypoelliptic diffusion.

Final results presented in Figures 4.3, 4.4, and 4.5 show a real improvement with respect to the results of the previous section and comparable with the state of the art.

All the examples presented in the following are obtained for images with a resolution of 256x256 pixels.

2 Hypoelliptic Diffusion

2.1 Images under consideration

Mathematically, a black-and-white image is a function $f: \Pi \rightarrow [0, 1]$, where Π is a square on the (x, y) -plane. If $f(x, y) = 0$ the color of the image at (x, y) is white, while if $f(x, y) = 1$ it is black. We will consider Π as a periodic subgroup of \mathbb{R}^2 endowed with its Haar measure.

Since the corresponding Haar measure is finite, all images are square integrable by definition. This also allows to consider images as Π -periodic functions $f: \mathbb{R}^2 \rightarrow [0, 1]$.

Together with the above continuous model we will consider also the corresponding discrete model: Physically, a black-and-white image f is stored as an $(M \times M)$ -matrix, where for simplicity we are assuming the same number of pixels vertically and horizontally. As before we assume $f_{kl} \in [0, 1]$, $k, l \in \{1, \dots, M\}$. Then, given a rectangular grid (x_k, y_l) , $k, l \in \{1, \dots, M\}$ in the (x, y) -plane, the discrete version of an image is the function $(x_k, y_l) \mapsto f(x_k, y_l) := f_{kl}$. As before, it is convenient to consider the grid and the functions to be periodic on \mathbb{Z}^2 .

Observe that we can assume that $f(x_k, y_l) > 0$ at any point (x_k, y_l) that corresponds to a non-corrupted pixel. Thus, due to the knowledge of the corrupted part, we can assume that $f(x_k, y_l) = 0$ when (x_k, y_l) corresponds to a corrupted pixel

2.2 Two models for the diffusion

2.2.1 Hypoelliptic diffusion in the continuous limit model

The main idea of the (continuous) model is then that V1 lifts images, which are Π -periodic functions $f: \mathbb{R}^2 \rightarrow [0, 1]$, to functions over the projective tangent bundle $PT\mathbb{R}^2$. This bundle has as base \mathbb{R}^2 and the projective line $P\mathbb{R}$ as fiber at (x, y) . Recall that $P\mathbb{R}$ is the set of directions of straight lines lying on the plane and passing through (x, y) , which can be represented by the angles $\theta \in [0, \pi]/\sim$ where the $0 \sim \pi$. In this model a corrupted image is reconstructed by minimizing the energy necessary to activate the regions of the visual cortex not excited by the image.

Mathematically speaking, the original image $f(x, y)$ is first smoothed through an isotropic Gaussian filter (it is widely accepted that this corresponds to an action at the retinal level, see [21, 22]). As shown [12] this yields a smooth function which is generically of Morse type, i.e., it has isolated non-degenerate critical points only. The smoothed image (that we will still call $f(x, y)$) is then lifted to the (generalized) function $\bar{f}(x, y, \theta)$ on $PT\mathbb{R}^2$ defined by

$$\bar{f}(x, y, \theta) := f(x, y) \delta(g(x, y, \theta)), \quad \text{for} \quad (2.1)$$

$$g(x, y, \theta) := \cos \theta \frac{\partial f}{\partial x}(x, y) + \sin \theta \frac{\partial f}{\partial y}(x, y), \quad (2.2)$$

where $\delta(\cdot)$ is the Dirac delta function. Moreover, the space $PT\mathbb{R}^2$, with coordinates $q = (x, y, \theta)$, is endowed with the sub-Riemannian structure with orthonormal frame given by the two vector fields

$$X_1(q) = \cos \theta \frac{\partial}{\partial x} + \sin \theta \frac{\partial}{\partial y}, \quad X_2(q) = \frac{\partial}{\partial \theta}. \quad (2.3)$$

This structure is invariant under the action of rigid motions. Via stochastic considerations (see [1]), one is then able to translate the energy minimizing principle expressed above to the fact that the image is evolved according to the hypoelliptic diffusion associated with the above vector fields. Namely, the reconstructed function on $PT\mathbb{R}^2$ is the solution $\psi = \psi(x, y, \theta, t)$ at time $t = 1$ of the initial problem

$$\frac{\partial \psi}{\partial t} = \Delta_H \psi, \quad \psi|_{t=0} = \bar{f}(x, y, \theta). \quad (2.4)$$

where, $\Delta_H := b(X_1)^2 + a(X_2)^2$ for some constant coefficients $a, b > 0$ to be chosen experimentally. We remark that this is equivalent to consider the solution ψ at time $t = \frac{b}{a}$ of (2.4) with $\Delta_H := (X_1)^2 + \frac{a}{b}(X_2)^2$. Finally, ψ is projected back to a function on \mathbb{R}^2 , which will be the final result of the image inpainting procedure. No boundary condition is needed in (2.4), since we are considering the diffusion on the whole space $PT\mathbb{R}^2$ and the initial function $\bar{f}(x, y, \theta)$ is periodic w.r.t. $(x, y, \theta) \in PT\mathbb{R}^2$.

Let us remark that, although in practice we will allow for an image-dependent tuning of the parameters a, b , in principle these coefficients are neurophysiological constants. Information about the initial image is fed to the evolution only through the initial condition \bar{f} .

2.2.2 Semi-discrete alternative to the hypoelliptic diffusion

In [1], we proposed a semi-discrete alternative to the Citti-Petitot-Sarti model, by assuming that the number N of directions represented in V1 is finite. The stochastic assumption of a Poisson process for the jumps between adjacent directions leads to the semi-discrete diffusion equation:

$$\frac{\partial \psi}{\partial t} = \Delta_{\mathcal{H}} \psi, \quad \psi|_{t=0} = \bar{f}(x, y, r), \quad (2.5)$$

where $\Delta_{\mathcal{H}} = bA + a\Lambda_N$ is the semi-discrete operator, where

$$A\Psi(x, y, r) = \left(\cos \theta_r \frac{\partial}{\partial x} + \sin \theta_r \frac{\partial}{\partial y} \right)^2, \\ \Lambda_N \Psi(x, y, r) = \Psi(x, y, r-1) - 2\Psi(x, y, r) + \Psi(x, y, r+1).$$

The limit of this diffusion operator when $N \rightarrow +\infty$ coincides in a suitable sense with the continuous operator Δ_H . This operator is invariant under the action of the semi-discrete rigid motions, with continuous translations and discrete rotations of angle $\theta_r = \frac{r\pi}{N}$.

2.2.3 Two distinct points of view, leading to similar computations

At this step, there are two possibilities for the integration of equation (2.5) starting from the lifts of the images described in Section 2.1. We may spatially discretize the

equation, or we may work with Fourier series assuming spatial periodicity of the initial condition \bar{f} . Both strategies lead to the same kind of fully-discrete equations. The second strategy leads to “exact” solutions under the periodicity assumption.

Working in the dual frequency grid to our spatial grid of Section 2.1, we are led to a completely decoupled set of M^2 linear ODE’s over \mathbb{C}^N of Mathieu type:

$$\frac{d\hat{\Psi}_{k,l}}{dt} = \frac{1}{2}(a\Lambda_N - bM\text{diag}_p(a_{k,l}^p)^2)\hat{\Psi}_{k,l}, \quad (2.6)$$

where $\hat{\Psi}_{k,l} = (\hat{\Psi}_{k,l}^1, \dots, \hat{\Psi}_{k,l}^N)$ and

$$(\Lambda_N \hat{\Psi}_{k,l}^r)_r = \frac{1}{2} \left(\hat{\Psi}_{k,l}^{r-1} - 2\hat{\Psi}_{k,l}^r + \hat{\Psi}_{k,l}^{r+1} \right), \\ a_{k,l}^p = \cos(\theta_p) \sin \left(2\pi \frac{k-1}{M} \right) + \sin(\theta_p) \sin \left(2\pi \frac{l-1}{M} \right).$$

We refer to [1] for details.

Each of the ODE’s (2.6) can be independently solved via standard numerical schemes such as the Crank-Nicolson scheme, recommended for this type of equation (see [23, Chapter 5]). Numerical experiments showed that no visible improvement is obtained by taking $N > 30$.

2.3 The algorithm

The algorithm will be divided in three steps:

1. Lift the image $f(x_k, y_l)$ to $\bar{f}(x_k, y_l, \theta_r)$.
2. Evolve $\bar{f}(x_k, y_l, \theta_r)$ according to (2.6) after passing to the dual frequency grid: $\bar{f} \mapsto \hat{\bar{f}}$. This step was already discussed in Section 2.2.3.
3. Go back to the spatial grid by inverse FFT and project the result back to the original 2 dimensional grid.

2.3.1 Lift

The discrete analogue of the initial function \bar{f} has the form:

$$\bar{f}(x_k, y_l, \theta_r) = \begin{cases} f(x_k, y_l), & \text{if } \theta_r \simeq \theta(k, l), \\ 0, & \text{if } \theta_r \not\simeq \theta(k, l). \end{cases} \quad (2.7)$$

Here, the formulation $\theta_r \simeq \theta(k, l)$ means that θ_r is the nearest point to $\theta(k, l)$ among all points of the grid $\{\theta_1, \dots, \theta_N\}$, and $\theta(k, l)$ is the discrete analogue of the slope angle of the level curve $f(x, y) = \text{const}$ passing through the point (x_k, y_l) . Namely, $\theta(k, l)$ is defined by the following formula:

$$\tan \theta(k, l) = -\frac{f_x}{f_y}(x_k, y_l), \quad (2.8)$$

where f_x and f_y are the standard finite-difference analogues of the corresponding partial derivatives. If $f_x(x_k, y_l) = f_y(x_k, y_l) = 0$ (which corresponds to a critical point of the Morse function) we define

$$\bar{f}(x_k, y_l, \theta_r) = \frac{f(x_k, y_l)}{N} \quad \text{for all } r = 1, \dots, N. \quad (2.9)$$

Generically, due to the Morse property, $|f_x| + |f_y| \neq 0$ at almost all points (x_k, y_l) and the function \bar{f} is defined by formulae (2.7) and (2.8). Thus the information about the initial image is contained in the both values $\theta(k, l)$ and $f(x_k, y_l)$.

2.3.2 Projection

The final step of our algorithm is to convert the result $\bar{F}(x_k, y_l, \theta_r)$ of the evolution into an image $F(x_k, y_l)$. A natural choice for $F(x_k, y_l)$ is the ℓ^p -norm of the function $\bar{F}(x, y, \theta)$ with respect to $\theta \bmod \pi$, where $1 \leq p \leq \infty$. As discussed in our previous paper [1], we have chosen the ℓ^∞ norm. Namely,

$$F(x, y) = \max_{\theta_r} \bar{F}(x, y, \theta_r). \quad (2.10)$$

After the projection, we obtain a positive function $F(x, y)$, whose maximal value, due to the action of the diffusion, is usually small. Therefore, it is necessary to renormalize.

2.4 Heuristic complements: SR/DR procedures

The above procedure has the drawback of applying the evolution to the whole image, and thus also on the non-corrupted part, blurring it. In [1], we proposed an heuristic complement to it, allowing to keep track of the initial information during the evolution. This method is based upon the general idea of distinguishing between the so-called *good* and *bad* points (pixels) of the image under reconstruction. Roughly speaking, the set G of good points consists of points that are already reconstructed enough (thus including non-corrupted points), while the set B of bad points consists of points that are still corrupted. This procedure then amounts to stopping, or at least slowing, the effects of the diffusion on G , without influencing B .

In [1], we described two possible implementation of this idea called *static restoration* (SR) and *dynamic restoration* (DR). The difference between the SR and the DR procedure consists in the way the sets of good and bad points are handled: in the SR procedure the set of good points coincides with the set of non-corrupted points and does not change during the diffusion, while in the DR procedure the set of good points coincides with the set of non-corrupted points only initially and bad points are allowed to become good through the action of the diffusion. At the end the algorithm including

the restoration procedure is iterated a certain number of times n . See [1] for details.

2.5 New experiments

In Figures 2.1 to 2.3 we present some experimental results related to the above mentioned methods. They concern only the hypoelliptic evolution, without the SR/DR procedures discussed in Section 2.4.

- The figure 2.1 shows the evolution of the diffusion in time, where the initial image is lifted according to (2.7)–(2.9).
- The figure 2.2 shows the anisotropic effect of the diffusion: The three processed images correspond to different kinds of lift. The first one is obtained with the trivial lift (formula (2.9)). The second processed image corresponds to a lift with the constant angle $\pi/4$ only, while the last one corresponds to a lift with the constant angle $3\pi/4$ only.
- The figure 2.3 is also connected to the effect of the lift: Here we lift to an image with constant gray levels but the gradient (the angle) is properly lifted.

On the other hand, we observed that when we apply the SR/DR procedures sufficiently often the effect of the lift itself is in fact neglectable. This may explain why, in the following heuristic developments, it is enough to use only the trivial lift, i.e., to lift the original image at all orientation values via formula (2.9). This is very important for highly and densely corrupted images, since it would be difficult to compute reasonable estimates of their gradients.

3 Modifications of the hypoelliptic diffusion

In this section we present the new idea of using a diffusion with varying coefficients in order to take more into account the knowledge of the corrupted part of the image.

3.1 Hypoelliptic diffusion with varying coefficients

One can try to modify (2.5) to take into account what we called good and bad points. Namely, we can consider the equation (2.5) where $\Delta_{\mathcal{H}} := bA + a\Lambda_N$ for some positive continuous coefficients $a(x, y)$, $b(x, y)$, through whom we can control the velocity of the diffusion as a function of the position. It is natural to choose smaller values of a, b at non-corrupted points and larger values at corrupted points.

The price to pay is that the essential decoupling effect from (2.5) to (2.6) does not take place anymore.

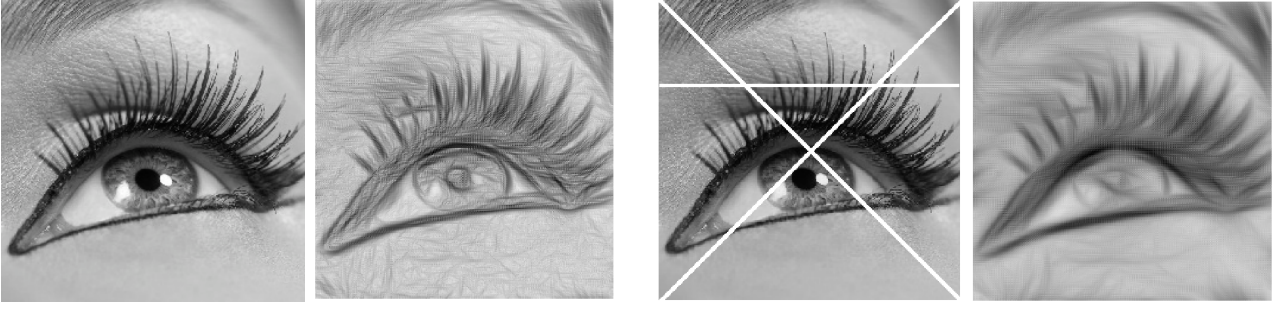


Figure 2.1: Two images showing the evolution of the diffusion with different final times. The functions are lifted according to (2.7)–(2.9)



Figure 2.2: Three reconstructions of the image to the left showing the anisotropic nature of the diffusion. The lift is taken to be, respectively the trivial one given by formula (2.9) at all points of the image, a lift with constant slope angle $\theta(k, l) \equiv \frac{\pi}{4}$ and a lift with constant slope angle $\theta(k, l) \equiv \frac{3\pi}{4}$.

To overcome this point we replace at each step of integration the varying coefficient version of (2.5) by a similar equation with constant coefficients. Namely, let $[t_i, t_{i+1}]$, $i = 0, \dots, N$, be the time interval of the integration and consider as initial datum the function $\psi_{i-1} = \psi(x, y, \theta, t_{i-1})$ calculated at the previous step (or the initial datum f if $i = 0$). Then, we replace the differential operator $\Delta_{\mathcal{H}}$ on the interval $[t_i, t_{i+1}]$ with the operator

$$\Delta'_{\mathcal{H}} := b'(X_1)^2 + a'(X_2)^2,$$

where a', b' are constant coefficients chosen as $a' = \max a(x, y)$ and $b' = \max b(x, y)$. Indeed, straightforward computations show that for $t_{i+1} - t_i$ sufficiently small the following approximation holds

$$\Delta_{\mathcal{H}}\psi \approx \Delta'_{\mathcal{H}}\psi - \Delta'_{\mathcal{H}}\psi_{i-1} + \Delta_{\mathcal{H}}\psi_{i-1} = \Delta'_{\mathcal{H}}\psi + d_i,$$

where d_i is the function on \mathbb{R}^2 defined by the last equality. Thus, on the segment $[t_{i-1}, t_i]$ we can replace (2.4) with the non-homogeneous equation

$$\frac{\partial \psi}{\partial t} = \Delta'_{\mathcal{H}}\psi + d_i, \quad t \in [t_{i-1}, t_i], \quad (3.1)$$

with constant coefficients a', b' and drift d_i .

After this approximation the decoupling effect mentioned in Section 2.2.3 persists and the Crank-Nicolson method is still pertinent applied to each of the decoupled ODE's.

3.1.1 Practical results

We define the coefficients $a(x, y)$ and $b(x, y)$ by the heuristic formulae

$$\begin{aligned} a(x, y) &= a_0 + a_1 \exp\left(-\frac{f^2(x, y)}{\sigma}\right), \\ b(x, y) &= b_0 + b_1 \exp\left(-\frac{f^2(x, y)}{\sigma}\right), \end{aligned} \quad (3.2)$$

where a_i, b_i, σ are constant parameters chosen experimentally. This choice corresponds to slowing down the diffusion at points with large values of $f(x, y)$.

We observe that for low levels of corruption, reconstruction of images with this method yields results which are comparable to, if not better than, the ones obtained through the SR/DR procedure. However, when the corrupted part becomes larger this method fails. This suggests that, in order to obtain a good inpainting algorithm for highly corrupted images, one has still to use

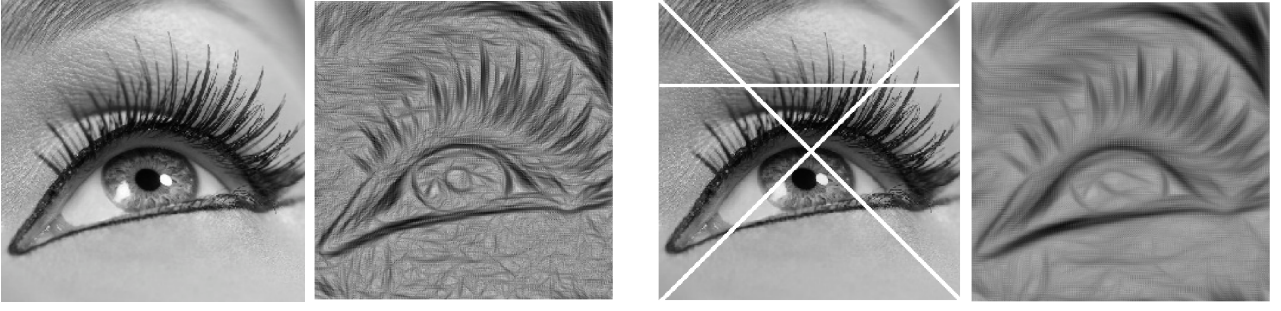


Figure 2.3: Two images showing the anisotropic nature of the diffusion. Here, the lifted function is computed through the gradient but then all the non-zero values are set to 0.5.

the SR/DR procedure, combining it with the varying coefficients.

In Figure 3.1, 3.2 and 3.3, we present three series of reconstructions obtained with the hypoelliptic diffusion with varying coefficients coupled with the DR procedure and using the trivial lift, i.e., defined by (2.9) at all points of the image. The last figure 3.3 of the series shows results with a high corruption rate.

4 AHE algorithm

Here, in order to improve on the results for high corruption rates, we were led to the Averaging and Hypoelliptic Evolution algorithm. The main idea behind the AHE algorithm is to try to provide the anisotropic diffusion with better initial conditions. More precisely, it is divided in the following 4 steps:

1. Preprocessing phase (Simple averaging);
2. Main diffusion (Strong smoothing);
3. Advanced averaging;
4. Weak smoothing.

Let us denote the sets of good and bad points by respectively G and B . Recall that initially $G = \{(x_k, y_k) \mid f(x_k, y_k) > 0\}$, $B = \{(x_k, y_k) \mid f(x_k, y_k) = 0\}$ and $B \cup G$ covers the whole grid. For each point $(x_k, y_l) \in B$ denote by Θ_{kl} its 9-points neighborhood. Also, define the set $G_{kl} = G \cap \Theta_{kl}$ and let $|G_{kl}|$ be the cardinality of G_{kl} ($0 \leq |G_{kl}| \leq 8$). We call ∂B the set of *boundary bad points*, i.e., of those $(x_k, y_l) \in B$ satisfying the condition $|G_{kl}| > 0$.

4.1 Step 1: Preprocessing phase (Simple averaging)

The aim of this phase is to fill in the corrupted areas of the picture with a rough approximation of what the reconstruction should be, through a discrete approximation

of an isotropic diffusion. Namely, we iteratively redefine the value of f at each boundary bad point (x_k, y_k) to be the average value of the good points in its 9-points neighborhood Θ_{kl} and then we remove (x_k, y_l) from B and add it to G .

More precisely, let $f^0 = f$, $G^0 = G$ and $B^0 = B$. Given f^i , G^i and B^i we then define f^{i+1} , G^{i+1} and B^{i+1} as follows. For any $(x_k, y_l) \in \partial B^i$ we put

$$f^{i+1}(x_k, y_l) = \frac{1}{|G_{kl}^i|} \sum_{(x, y) \in G_{kl}^i} f^i(x, y), \quad (4.1)$$

and for any $(x_k, y_l) \notin \partial B^i$ we put

$$f^{i+1}(x_k, y_l) = f^i(x_k, y_l).$$

Observe, in particular, that this formula leaves the values of f^{i+1} on $B^i \setminus \partial B^i$ to be zero. Finally, $G^{i+1} = G^i \cup \partial B^i$ and $B^{i+1} = B^i \setminus \partial B^i$.

Since the set $\partial B^i = \emptyset$ if and only if $B^i = \emptyset$, after a finite number of step s we will obtain $B^s = \emptyset$. We will then let $g = f^s$ to be the result of this procedure. Observe that, in particular, $g(x_k, y_l) > 0$ for all (x_k, y_l) .

It turns out that the reconstructed image g presents a “mosaic” effect, which is more stronger for highly corrupted images (see Fig. 4.1, center). It should be noted that such phenomena arises also for other reconstruction procedures based on averaging procedures, as the median filter [24] (see fig. 4.1, right).

Remark 4.1. We tested many possible alternative procedures for this step. However, none of these yielded results as good as the very elementary procedure we described above.

4.2 Step 2: Main diffusion (Strong smoothing)

The goal of this step is elimination (or at least weakening) of the “mosaic” effect resulting from the previous step. Here, we apply the hypoelliptic diffusion (2.5) with

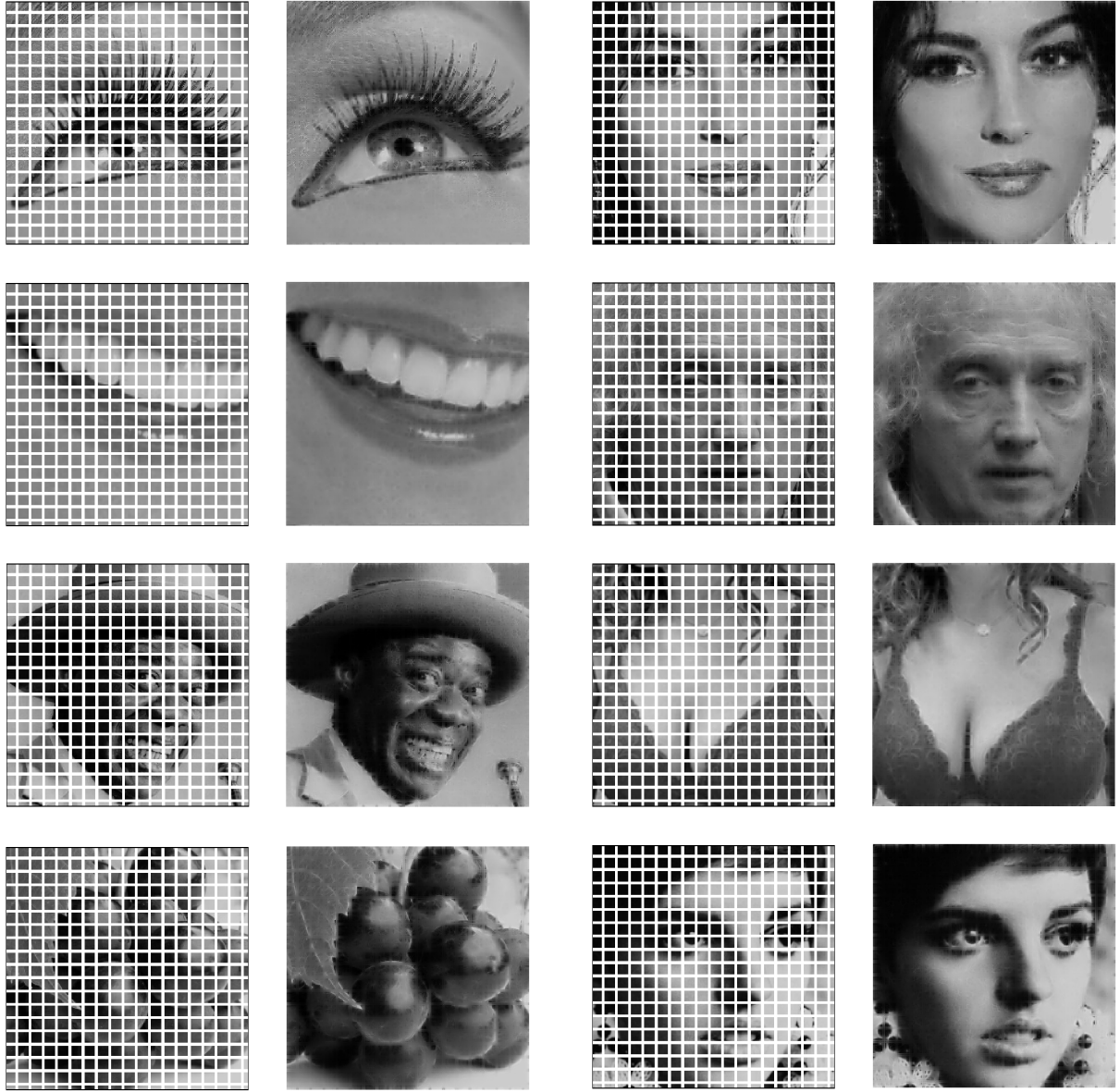


Figure 3.1: Images reconstructed with the hypoelliptic equation with varying coefficients and the DR procedure, Section 3.1.1. Total corruption: 37%, width of corrupted lines: 3 pixels. Parameters in (3.2): $a_0 = 1.1$, $a_1 = 10$, $b_0 = 0.1$, $b_1 = 0.4$, $\sigma = 0.1$. Parameters of the DR procedure: $n = 50$, $\epsilon = 0.1$.

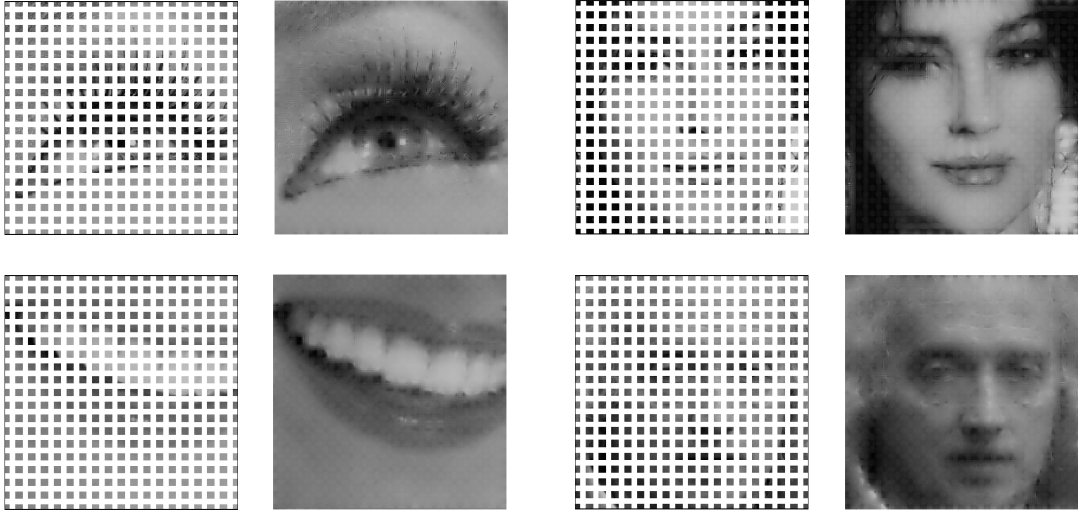


Figure 3.2: Images reconstructed with the hypoelliptic equation with varying coefficients and the DR procedure, Section 3.1.1. Total corruption: 67%, width of corrupted lines: 6 pixels. Parameters in (3.2): $a_0 = 2.3$, $a_1 = 20$, $b_0 = 1.5$, $b_1 = 6.6$, $\sigma = 0.1$.

varying coefficients $a = a(x, y)$ and $b = b(x, y)$ chosen so that the diffusion is more intensive at the points where the “mosaic” effect is more strong. Obviously, the diffusion should be as weak as possible elsewhere.

To estimate the intensity of the “mosaic” effect, we use the absolute value of the gradient of the function g . Indeed, comparing the first two images presented on Figure 4.2, one can see that most of the points with strong “mosaic” effect coincide with the points where $|\nabla g(x, y)|$ is large.

Thus we apply the hypoelliptic diffusion (2.5) with initial condition $\bar{g}(x, y, \theta)$, obtained by the trivial lift given by the formula (2.9), and coefficients $a = a(x, y)$ and $b = b(x, y)$ defined by the empirical formula

$$\begin{aligned} a(x, y) &= a_0 + a_1 \exp\left(-\frac{\varphi^2(x, y)}{\sigma}\right), \\ b(x, y) &= b_0 + b_1 \exp\left(-\frac{\varphi^2(x, y)}{\sigma}\right), \\ \text{where } \varphi(x, y) &= 1 - \frac{|\nabla g(x, y)|}{\max |\nabla g|}. \end{aligned} \quad (4.2)$$

Here, a_i, b_i, σ are constant parameters experimentally chosen. In all restorations presented in this section, we used the following values:

$$a_0 = 0.55, \quad a_1 = 5, \quad b_0 = 0.05, \quad b_1 = 0.2, \quad \sigma = 0.4.$$

From the practical point of view, the gradient $\nabla g(x, y)$ is replaced by its finite-difference approximation.

We remark that the choice of the trivial lift given by (2.9) in this situation presents an obvious advantage. Indeed, if we were using (2.7)–(2.8) we would lift along the

directions that coincide with the boundaries of the “mosaic” effect. This would force the diffusion to follow such boundaries, thus preventing the smoothing effect. Therefore we prefer to control the intensities of the diffusion via the varying coefficients a, b only.

4.3 Step 3: Synthesis (Advanced averaging)

As can be seen in the central image of Figure 4.2, right, after the second step of the algorithm we remove the “mosaic” effect. However, the diffusion introduces a blurring effect, that cannot be removed by decreasing the coefficients a, b , since this yields images still presenting the “mosaic” effect. To pass between this Scylla and Charybdis, we then make a synthesis of the images obtained after the first and the second steps.

As before, let $f(x, y)$ be the function of the initial corrupted image, and B, G be the corresponding sets of good and bad points. Recall that we denoted by $g(x, y)$ the function obtained after the first step and let $h(x, y)$ denote the function obtained after the second step.

The structure of step 3 is similar to the one of step 1. Indeed, we will apply an iterative procedure aimed to reconstruct the bad points of f using information from the good points and the function h . The only difference between steps 1 and 3 is that when $(x_k, y_l) \in \partial B^i$, we define $f^{i+1}(x_k, y_l)$ as

$$f^{i+1}(x_k, y_l) = \arg \min_{X \in [0, 1]} \sum_{(x, y) \in G_{kl}^i} \left| \frac{X}{f^i(x, y)} - \frac{h(x_k, y_l)}{h(x, y)} \right|^2. \quad (4.3)$$

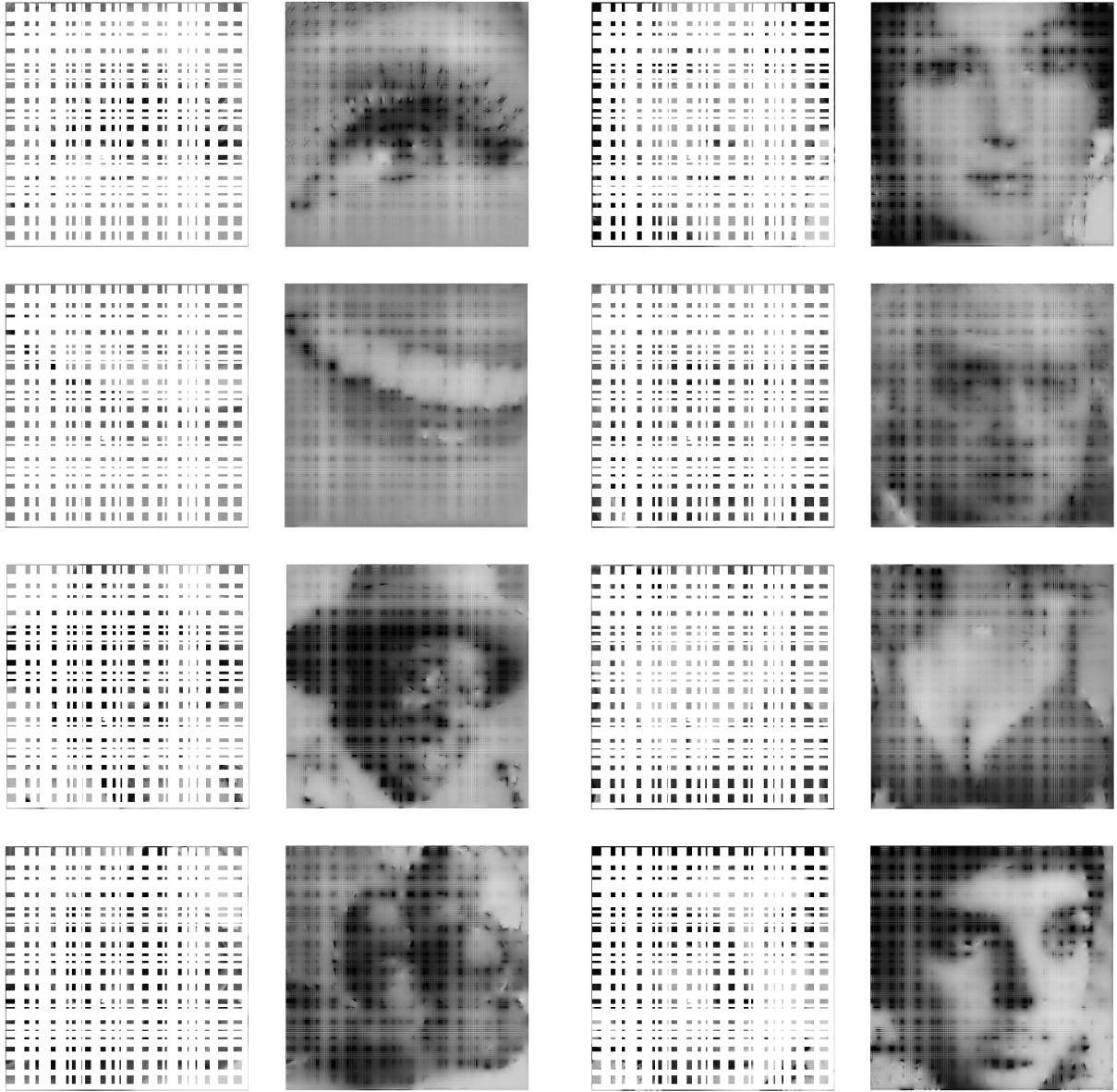


Figure 3.3: Images reconstructed with the hypoelliptic equation with varying coefficients and the DR procedure, Section 3.1.1. Total corruption: 85%. Parameters in (3.2): $a_0 = 1.1$, $a_1 = 10$, $b_0 = 0.1$, $b_1 = 0.4$, $\sigma = 0.1$. Parameters of the DR procedure: $n = 100$, $\epsilon = 1.0$.



Figure 4.1: The second (left group) and the third (right group) corrupted images from Figure 3.3 as reconstructed after step 1 (left) and the same images reconstructed with the median filter (right).

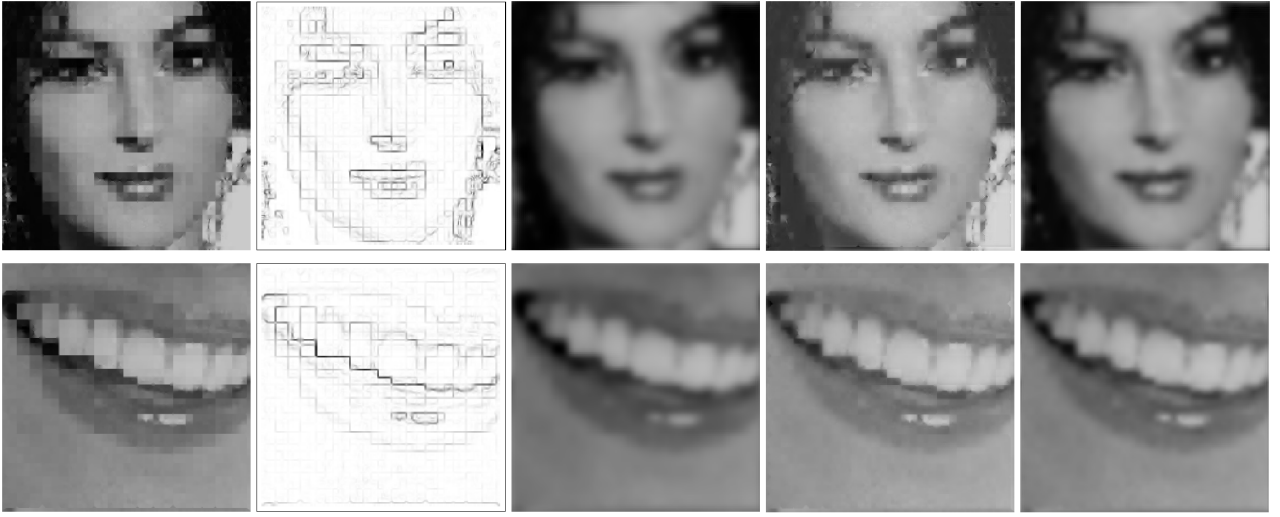


Figure 4.2: The second (first row) and the third (second row) corrupted images from Figure 3.3 after each step of the AHE algorithm. The second image depicts the modulus of the gradient of the result of step 1, which we use to compute the varying coefficients in step 2.

This expression realizes a compromise between the averaging and the diffusion. The above formula is well defined since $f(x, y) > 0$ for all $(x, y) \in G_{kl}^i$ and the smoothed function $h(x, y)$ is always strictly positive. Moreover, the expression in the right-hand side of (4.3) is a continuous convex function of X , and thus the minimum exists. A straightforward computation allows then to compute explicitly (4.3) as

$$f^{i+1}(x_k, y_l) = h(x_k, y_l) \frac{\sum_{(x,y) \in G_{kl}^i} f^i(x, y)^{-1} h(x, y)^{-1}}{\sum_{(x,y) \in G_{kl}^i} f^i(x, y)^{-2}}.$$

The results of this reconstruction are presented in the fourth image of Figure 4.2.

4.4 Step 4: Weak smoothing

Clearly step 3, as step 1, reintroduces a little “mosaic” effect. Then, we essentially repeat step 2. The only difference is that now we use a weaker diffusion.

In all the reconstructed images presented below we use the hypoelliptic diffusion (2.5) with varying coefficients $a = a(x, y)$ and $b = b(x, y)$ defined by formula (4.2). We use the parameters

$$a_0 = 0.75, \quad a_1 = 1.5, \quad b_0 = 0.015, \quad b_1 = 0.1, \quad \sigma = 0.3.$$

4.5 Conclusion

Comparing the results in Figures 3.1, 3.2 and 3.3 with those in Figures 4.3, 4.4 and 4.5, respectively, one can see that the method presented in the last section provides better results. In particular, the performances of this method are specially better for highly corrupted images.

Acknowledgments

We deeply thank S. Masnou for his help and for having kindly accepted to apply his methods to some of our images for the purpose of comparison.

References

- [1] U. Boscaín, R. A. Chertovskih, J. P. Gauthier, and A. O. Remizov, “Hypoelliptic diffusion and human vision: a semidiscrete new twist,” *SIAM J. Imaging Sci.*, vol. 7, no. 2, pp. 669–695, 2014.
- [2] A. Bugeau, M. Bertalmío, V. Caselles, and G. Sapiro, “A comprehensive framework for image inpainting,” *IEEE Trans. Image Process.*, vol. 19, pp. 2634–45, Oct. 2010.
- [3] M. Bertalmio, G. Sapiro, V. Caselles, and C. Ballester, “Image inpainting,” in *Proc. of SIGGRAPH 2000, New Orleans, USA, July, 2000*.
- [4] T. Chan, S. Kang, and J. Shen, “Euler’s elastica and curvature-based inpainting,” *SIAM J. Appl. Math.*, 2002.
- [5] S. Masnou and J.-M. Morel, “Level lines based disocclusion,” in *Image Processing, 1998. ICIP 98. Proceedings. 1998 International Conference on*, vol. 3, pp. 259–263, 1998.
- [6] M. Wang, B. Yan, and K. N. Ngan, “An efficient framework for image/video inpainting,” *Signal Process. Image Commun.*, 2013.

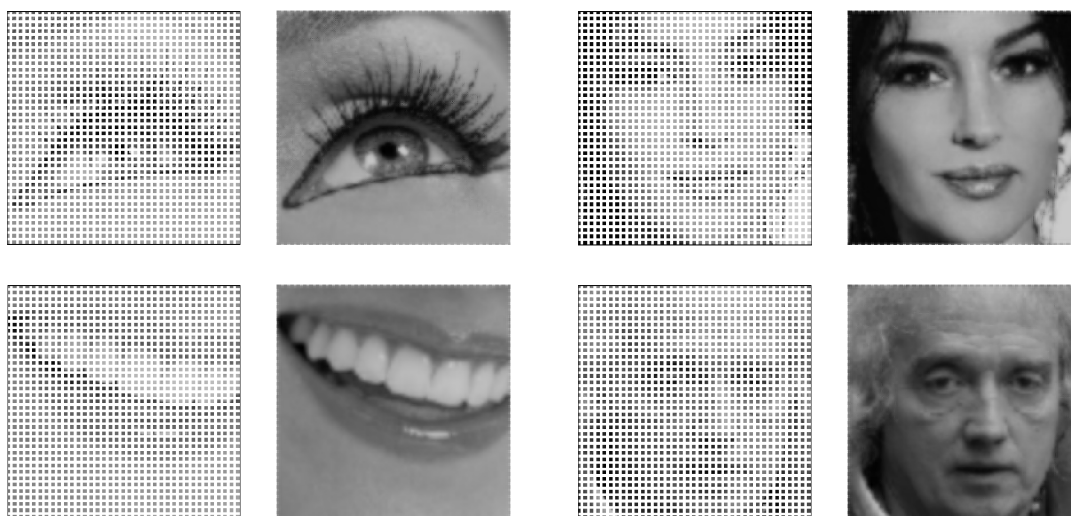


Figure 4.3: Images reconstructed with the AHE algorithm, Section 4. Total corruption: 67%, width of corrupted lines: 3 pixels.

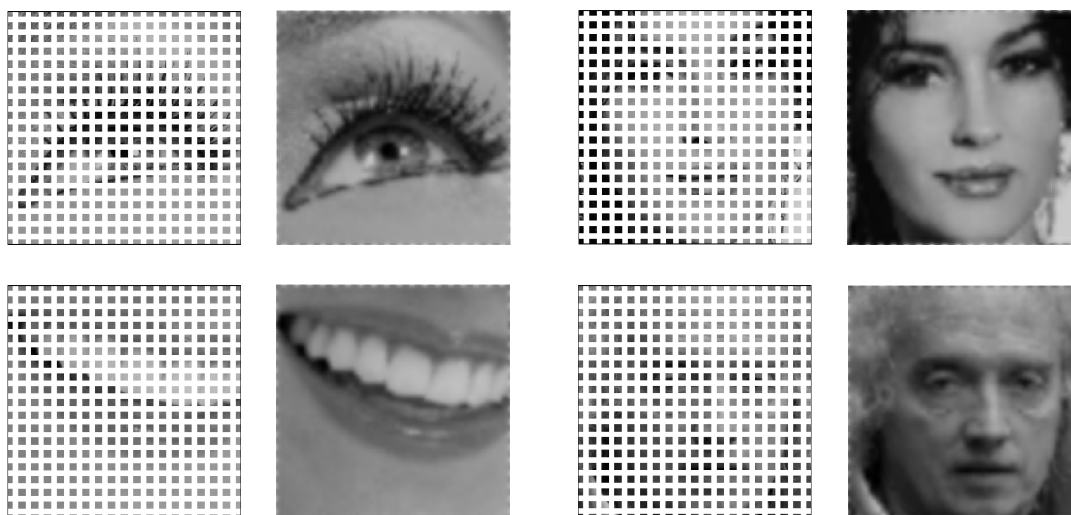


Figure 4.4: Images reconstructed with the AHE algorithm, Section 4. Total corruption: 67%, width of corrupted lines: 6 pixels.

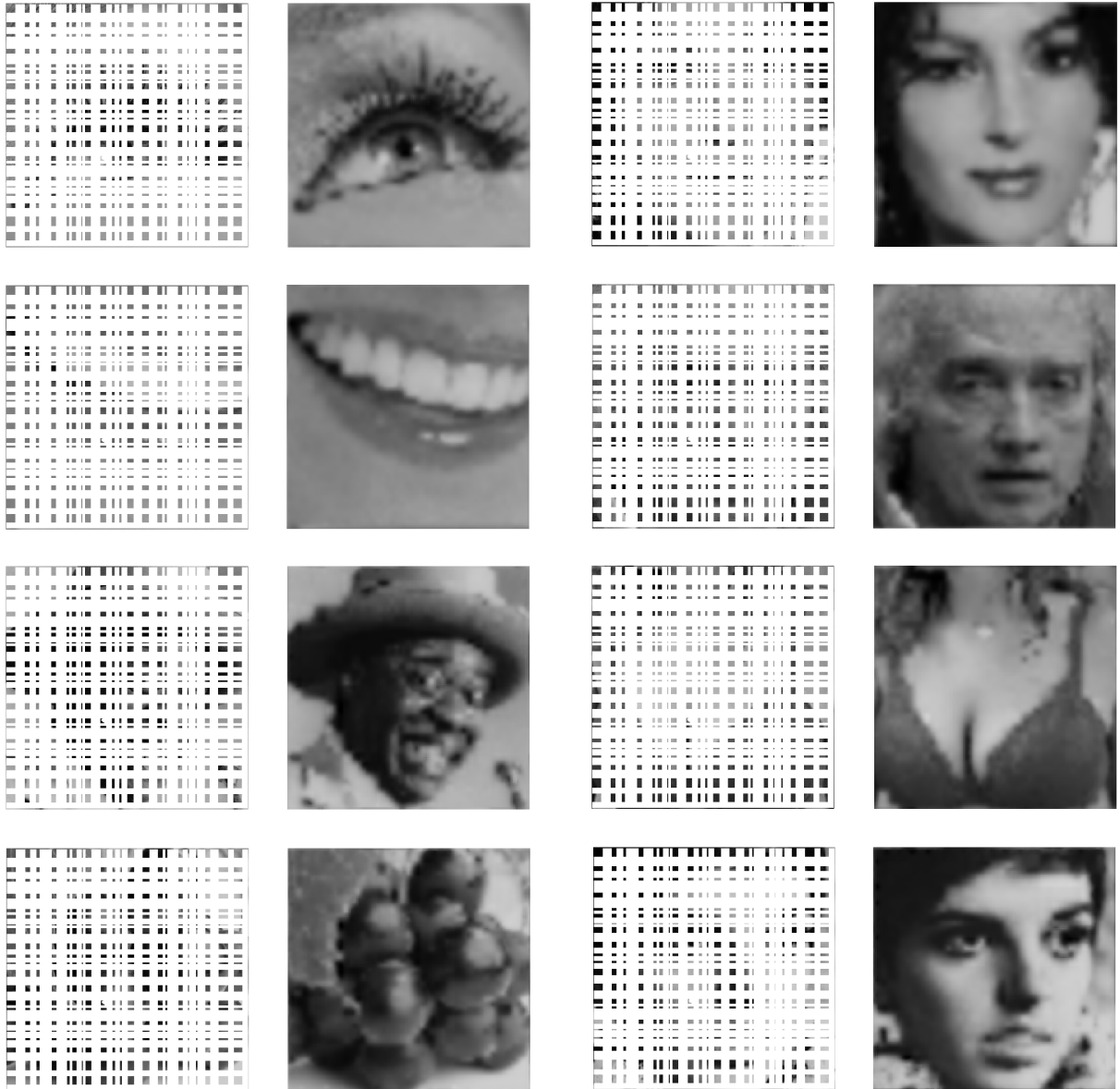


Figure 4.5: Images reconstructed with the AHE algorithm, Section 4. Total corruption: 85%.

- [7] J. Petitot, *Neurogéométrie de la vision - Modèles mathématiques et physiques des architectures fonctionnelles*. Les Éditions de l'École Polytechnique, 2008.
- [8] J. Petitot, "The neurogeometry of pinwheels as a sub-Riemannian contact structure," *J. Physiol. Paris*, vol. 97, no. 2-3, pp. 265–309, 2003.
- [9] G. Citti and A. Sarti, "A Cortical Based Model of Perceptual Completion in the Roto-Translation Space," *J. Math. Imaging Vis.*, vol. 24, pp. 307–326, Feb. 2006.
- [10] G. Sanguinetti, G. Citti, and A. Sarti, "Image completion using a diffusion driven mean curvature flow in a sub-riemannian space," in *Proceedings of the 3rd International Conference on Computer Vision Theory and Applications (VISAPP 2008)*, vol. 2, pp. 46–53, 2008. Funchal, Portugal, 2008.
- [11] U. Boscain, G. Charlot, and F. Rossi, "Existence of planar curves minimizing length and curvature," *Tr. Mat. Inst. Steklova*, vol. 270, no. Differentsialnye Uravneniya i Dinamicheskie Sistemy, pp. 49–61, 2010.
- [12] U. Boscain, J. Duplaix, J.-P. Gauthier, and F. Rossi, "Anthropomorphic image reconstruction via hypoelliptic diffusion," *SIAM J. Control Optim.*, pp. 1–25, 2012.
- [13] U. Boscain, R. Duits, F. Rossi, and Y. Sachkov, "Curve cusplless reconstruction via sub-Riemannian geometry," *ESAIM Control Optim. Calc. Var.*, vol. 20, no. 3, pp. 748–770, 2014.
- [14] R. Duits and M. A. van Almsick, "The explicit solutions of linear left-invariant second order stochastic evolution equations on the 2D euclidean motion group," in *Quart. Appl. Math.*, no. 66, pp. 27–67, 2008.
- [15] R. Duits and E. Franken, "Left-invariant parabolic evolutions on $SE(2)$ and contour enhancement via invertible orientation scores Part I: linear left-invariant diffusion equations on $SE(2)$," *Quart. Appl. Math.*, vol. 68, no. 2, pp. 255–292, 2010.
- [16] R. Duits and E. Franken, "Left-invariant parabolic evolutions on $SE(2)$ and contour enhancement via invertible orientation scores Part II: nonlinear left-invariant diffusions on invertible orientation scores," *Quart. Appl. Math.*, vol. 68, no. 2, pp. 293–331, 2010.
- [17] R. K. Hladky and S. D. Pauls, "Minimal surfaces in the roto-translation group with applications to a neuro-biological image completion model," *J. Math. Imaging Vision*, vol. 36, no. 1, pp. 1–27, 2010.
- [18] D. Hubel and T. Wiesel, "Receptive fields of single neurones in the cat's striate cortex," *J. Physiol.*, vol. 148, pp. 574–591, 1959.
- [19] U. Boscain, J.-P. Gauthier, D. Prandi, and A. Remizov, "Image reconstruction via non-isotropic diffusion in Dubins/Reed-Shepp-like control systems," in *53rd IEEE Conference on Decision and Control*, pp. 4278–4283, 2014.
- [20] S. Masnou, "Disocclusion: a variational approach using level lines," *Image Process. IEEE Trans.*, 2002.
- [21] D. Marr and E. Hildreth, "Theory of edge detection," *Proc. R. Soc. Lond. B. Biol. Sci.*, vol. 207, no. 1167, pp. 187–217, 1980.
- [22] L. Peichl and H. Wässle, "Size, scatter and coverage of ganglion cell receptive field centres in the cat retina," *J. Physiol.*, vol. 291, pp. 117–141, 1979.
- [23] G. Marchuk, *Methods of Numerical Mathematics*. Springer-Verlag, 1982.
- [24] T. Huang, G. Yang, and G. Tang, "A fast two-dimensional median filtering algorithm," *IEEE Trans. Acoust.*, vol. 27, no. 1, 1979.